



3D in situ stress state modelling and fault reactivation risk exemplified in the Ruhr region (Germany)

Michal Kruszewski^{a,b,*}, Giordano Montegrossi^c, Martin Balcewicz^{b,d},
Gabriela de Los Angeles Gonzalez de Lucio^e, Onyedika Anthony Igbokwe^{b,f},
Tobias Backers^b, Erik H. Saenger^{d,a,b}

^a Fraunhofer Research Institution for Energy Infrastructures and Geothermal Systems IEG, Am Hochschulcampus 1 IEG, 44801 Bochum, Germany

^b Institute of Geology, Mineralogy, and Geophysics, Ruhr-University Bochum, Universitätsstraße 150, 44801 Bochum, Germany

^c Institute of Geoscience and Earth Resources, National Research Council of Italy, Via G. La Pira 4, 50121 Firenze, Italy

^d Department of Civil and Environmental Engineering, Bochum University of Applied Sciences, Am Hochschulcampus 1, 44801 Bochum, Germany

^e Geologischer Dienst NRW, De-Greif-Str. 195, 47803 Krefeld, Germany

^f Department of Physics, Geology and Geophysics, Alex Ekwueme Federal University Ndufu-Alike, Ikwo, P.M.B. 1010, Abakaliki, Ebonyi State, Nigeria

ARTICLE INFO

Article history:

Received 22 February 2022

Received in revised form 7 July 2022

Accepted 28 July 2022

Available online 3 August 2022

Editors-in-Chief:

Professor Lyesse Laloui and Professor Tomasz Hueckel

Dataset link: dx.doi.org/10.24406/fordatis/205

Keywords:

Reservoir geomechanics
Geomechanical modelling
Geothermal geomechanics
Numerical modelling
Fault reactivation risk
Sedimentary geothermal systems
Ruhr region

ABSTRACT

Throughout the 700-yearlong coal exploration period in the Ruhr region, an abundance of geological, geophysical, seismic, and in situ stress data was obtained from the Carboniferous strata. In this study, we take advantage of this unique dataset to develop a static 3D geomechanical model to predict the spatially continuous distribution of undisturbed in situ stress state and evaluate the reactivation risk of major fault zones. Compared to the point-wise stress information, the spatially continuous in situ stress state provides an effective tool for planning subsurface operations and assessing seismic hazards in areas where no stress information is available. The developed model was validated against a comprehensive calibration dataset including results from geophysical logging, borehole deformation, and fault-slip analysis, in situ hydrofracturing measurements, distribution of subsidence, microseismicity, and observations from coal mining activities. Consequently, interpretation and assessment of the model results including their uncertainties, reliability, limitations, and perspectives are discussed. The possible applications of the model approach for seismic hazard prediction and utilization of deep geothermal energy in the Ruhr region are outlined.

© 2022 The Authors. Published by Elsevier Ltd. This is an open access article under the CC BY license (<http://creativecommons.org/licenses/by/4.0/>).

1. Introduction

Geothermal systems rely either on fluid-filled and permeable rock formations and faults (i.e., hydrothermal systems), or impermeable rock formations, which, under a concept of an engineered geothermal system (EGS), are stimulated prior to the heat extraction. The development of both systems, by altering initial pore pressure, will change the stress state of the host rock and may induce seismic activity. The quantification of the critical stress state is of importance for identifying suitable and safe areas for the efficient utilization of geothermal energy resources. To investigate the stress state, three elements have to be

addressed: (i) undisturbed initial in situ stress state, (ii) rock's and fault's failure criteria, and (iii) man-made spatio-temporal pore pressure changes due to during drilling, fluid injection, or production operations.¹ The two latter elements are a focus of many scientific studies (e.g., Refs. 2–4), whereas the quantification of the undisturbed in situ stress state remains most often highly uncertain.

3D geomechanical models, providing critical a priori in situ stress tensor information, are used for safe and sustainable exploration and exploitation of geothermal and hydrocarbon resources (e.g., Refs. 5–9). Examples include applications for (i) predicting borehole stability (e.g., Refs. 10–12), (ii) selecting drill paths and drilling targets (e.g., Refs. 13, 14), (iii) designing reservoir stimulation operations (e.g., Refs. 15, 16), (iv) assessing reactivation potential of fractures and faults (e.g., Refs. 3, 17), (v) addressing reservoir depletion (e.g., Refs. 18, 19), (vi) evaluating compaction, subsidence, and casing shear issues (e.g.,

* Corresponding author at: Fraunhofer Research Institution for Energy Infrastructures and Geothermal Systems IEG, Am Hochschulcampus 1 IEG, 44801 Bochum, Germany.

E-mail address: michal.kruszewski@ieg.fraunhofer.de (M. Kruszewski).

Refs. 20–22), and (vii) investigating hazards related to induced seismicity (e.g., Ref. 23).

Throughout the 700-yearlong coal exploration period in the Ruhr region, an abundance of geological, geophysical, and in situ stress data has been obtained from the Carboniferous strata up to depths crucial for the coal mining industry. In this study, we take advantage of this unique dataset for development of a static 3D geomechanical model to predict the spatially continuous distribution of in situ stress state and evaluate the reactivation risk of major fault zones. The model, with a total area of 827 km² is located in the central part of the Ruhr region and reaches vertical depths of 6 km. For the calibration of the numerical model developed with COMSOL Multiphysics software,²⁴ we use a comprehensive model-independent dataset including (i) geophysical logging results, (ii) in situ measurements of horizontal stress magnitudes, and (iii) borehole deformation analyses. Additionally, results from the fault-slip analysis, distribution of microseismicity, subsidence, and localized permeability indicators from coal mining were utilized to confirm model robustness.

2. Study area

2.1. Geological setting and paleostress

The Ruhr region (North Rhine-Westphalia, Germany), located to the north of the Rhenohercynian Massif, is a result of the Hercynian orogeny and a classical foreland basin (e.g., Ref. 25). It consists mainly of interbedded sequences of sand, clay, silt, and coal layers (i.e., cyclothemes) of Upper Carboniferous age. The coal-bearing Upper Carboniferous strata in the Ruhr region is divided into the stratigraphic units of Namurian C to Westphalian A–C (e.g., Ref. 26). The folded layers of the Upper Carboniferous are overlain by a weakly north-dipping, angular unconformity from the Upper Cretaceous. The southern limit of the Cretaceous layers is along the line of the cities Essen, Bochum, and Dortmund. Towards the north, the layers of Cretaceous age increase continuously in thickness until finally reaching about 1.8 km thickness in the Münsterland Cretaceous Basin (e.g., Ref. 27). In total, the thickness of the coal-bearing strata is about 2.9 km. In the South of the Ruhr region, at the margin of the Rhenohercynian Massif, Devonian carbonates are assumed to be present below the coal-bearing Upper Carboniferous strata at a depth of about 5 km.²⁸

The Ruhr region is dominated by two sets of regional fault zones oriented (i) NW-SE to NNW-SSE with dip angles $\geq 80^\circ$ and (ii) NE-SW with dip angles between 60 and 80° (e.g., Refs. 25, 29). Highly complex fold structures with a mean ENE-WSW strike direction are also observed in the region (e.g., Ref. 30).

Outcrop studies in the south Ruhr region have shown that in the Devonian carbonates similar discontinuity orientations as in the coal-bearing Upper Carboniferous strata can be expected.³⁴ As an example, in the outcrops of the Steltenberg quarry (Fig. 1a), mesoscale fault zones encompass several bed-perpendicular and sub-parallel faults. The shear displacement is observed from the offset of bed boundaries and/or slickensides. The first fault network comprises of large sub-horizontal ENE-WSW-striking thrust fault, which dips approximately 20 to 35° to the bedding and is 3 to 5 m wide. Intensely fractured rocks with cores defined by high-strain fault rocks, including non-cohesive and cohesive crush breccia, characterize the narrow-range damage zones of this fault zone (Fig. 2f, g, h), which is expected to be a subsidiary of the Ennepe thrust developed during the Hercynian orogeny.^{35,36} The second fault network is NNW-SSE-striking, has a high dip (from 60 to 75°), and is six times wider (40 m) than the ENE-WSW-striking network, locally reaching 50 m (Fig. 2a, b). The inner core contains 5 m thick clay gouge and/or cohesive crush breccias. The NNW-SSE fault network forms in a conjugate pattern as a result

of the NW-SE acting sub-horizontal compression (Fig. 2c, d, e), and overprints the ENE-WSW-striking fault network (Fig. 2a).

2.2. Past geomechanical studies

The in situ stress state of the Ruhr region was investigated in a few surveys, performed predominantly in its northern parts with hydrofracturing and overcoring methods (Fig. 3). Measurements were carried out from the 1970s to the 2000s to optimize the design of crosscuts and mine layouts and, later on, to evaluate stress state in coal bed methane wells (i.e., Refs. 38–44). Most of the in situ measurements in the Ruhr region were limited to depths of interest for the coal mining industry (i.e., ~ 1.5 km).

In the last 40 years more than 1000 modern exploration boreholes were drilled in the northern part of the Ruhr region.⁴⁵ This immense database allowed for detailed analysis of borehole elongations and interpretation of the maximum horizontal stress azimuth, θ_{SHmax} . A total length of 761 m of borehole breakouts from 3.95 km of analysed four-arm caliper logs in 40 boreholes spread across the Ruhr region were analysed by Ref. 39. The mean θ_{SHmax} from his study is $149 \pm 36^\circ$. Reinecker et al.⁴⁶ discriminated borehole breakouts in 51 boreholes in the Ruhr region with a total breakout length of 3.01 km. The length-weighted θ_{SHmax} amounted to $168 \pm 48^\circ$. The great majority of θ_{SHmax} data in the Ruhr region is of low quality (i.e., D and E quality category of stress indicator based on World Stress Map stress quality ranking) and, thus, less reliable.⁴⁷ Only a few measurements of higher quality (i.e., B and C quality category of stress indicator) were registered in the region. Few measurements, from which the majority being of low quality, indicate NE-SW orientation of θ_{SHmax} , and being, thus, perpendicular to the regional θ_{SHmax} .⁴⁸

Based on the existing data, the Ruhr region can be separated into two main stress units in terms of θ_{SHmax} with the boundary being located at the General Blumenthal mine (Fig. 3). The eastern stress unit is characterized by θ_{SHmax} transition from the NNW-SSE direction in its most eastern parts (i.e., mine Westfalen) to NW-SE direction at the location of Haus Aden and Heinrich-Robert mines. These θ_{SHmax} are likely to be the result of regional faulting of the coal-bearing strata.⁴³ The western stress unit is characterized by θ_{SHmax} ranging from N-S direction at the location of Lohberg and General Blumenthal mines, and then reorientation from NNW-SSE to NW-SE direction at the location of Friedrich Heinrich and Niederberg mines. These θ_{SHmax} are supposedly influenced by the graben structure of the Lower Rhine Bay.⁴³ Based on results from in situ stress testing by Refs. 39–44 it can be stated that the Ruhr region is dominated by a strike-slip regime with magnitude of minimum horizontal stress, S_{hmin} , being smaller than the vertical stress magnitude, S_v . No natural seismicity has been recorded in the Ruhr region to derive the stress regime from focal mechanisms.^{49,50}

3. Simulation approach

To simulate the 3D state of the in situ stress a two-step approach following the methodology developed in Refs. 6, 51 was utilized. As a first step, the initial stress state, in the absence of tectonic loading, was established. This procedure, which ensures an appropriate ratio of horizontal-to-vertical effective stresses, was performed assuming no lateral tectonic loading with vertical and lateral stresses being controlled by gravitational forces only. Effective horizontal stresses, σ_h , being represented by a function of body forces of the cumulative weight of the overlying model layers and their Poisson's ratios, ν , which, according to the principles of linear elasticity amount to

$$\sigma_h = \sigma_v \cdot \frac{\nu}{(1 - \nu)} \quad (1)$$

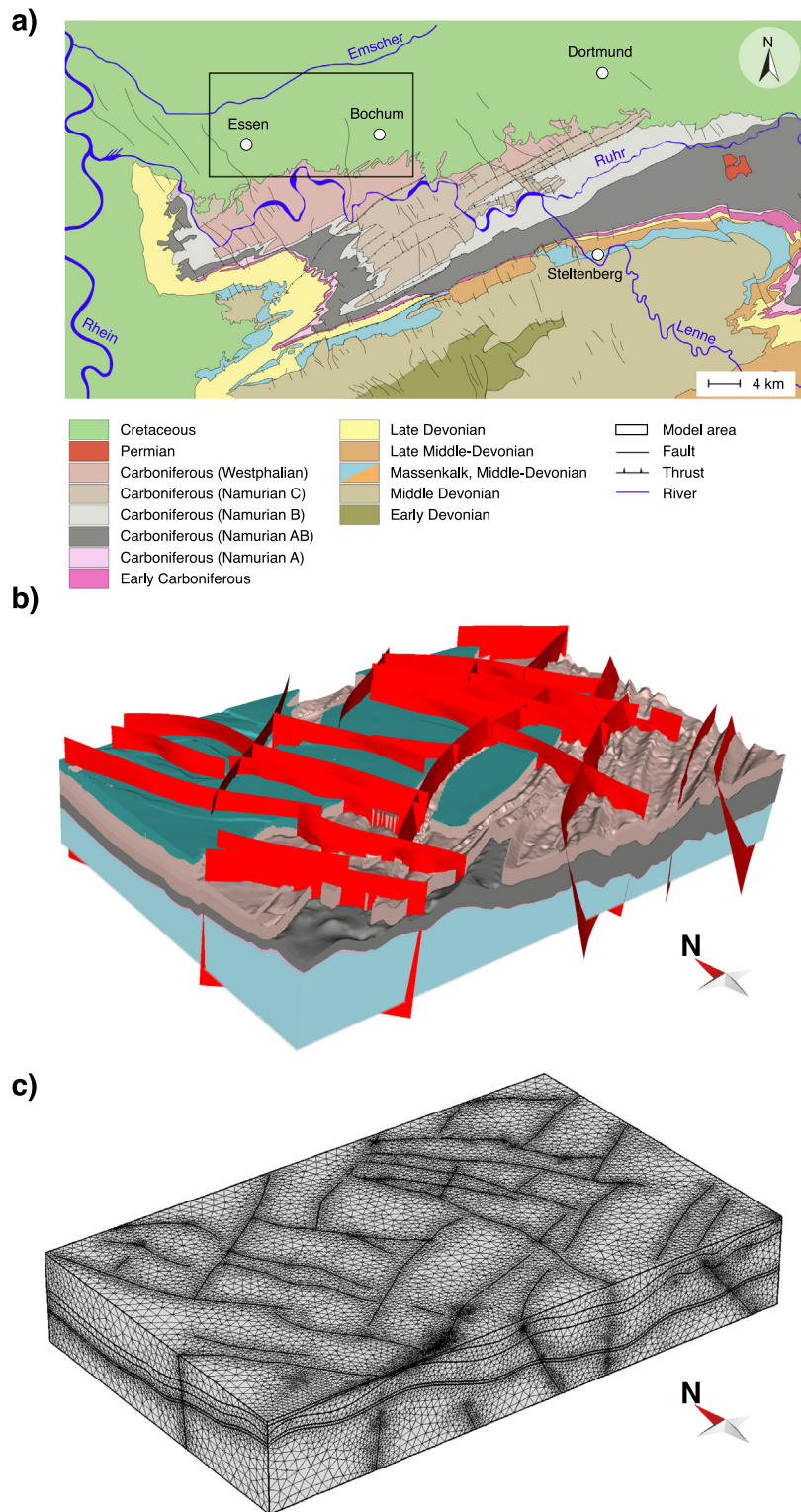


Fig. 1. The workflow of a static 3D geomechanical model: (a) simplified geological map of the Rhine-Ruhr area (after Ref. 31 and Ref. 32); (b) 3D structural-geological model; (c) discretization of the model geometry in the FEM environment.

where, σ_v is the effective vertical stress. During gravity generation, undesirable gravity-induced settlement occurs within the model volume. To remove these displacements, the stress state with the gravity-induced settlement was implemented into an undeformed model, and with two equilibration iteration steps (with results from a first iteration being used as a starting point

in the second iteration), gravitational displacements were removed. In the last iteration, displacements were minimized to a few centimetres with maximum displacements reaching few metres.

Once the initial stress state was equilibrated with gravitational forces and gravity-driven subsidence removed, in a second step,

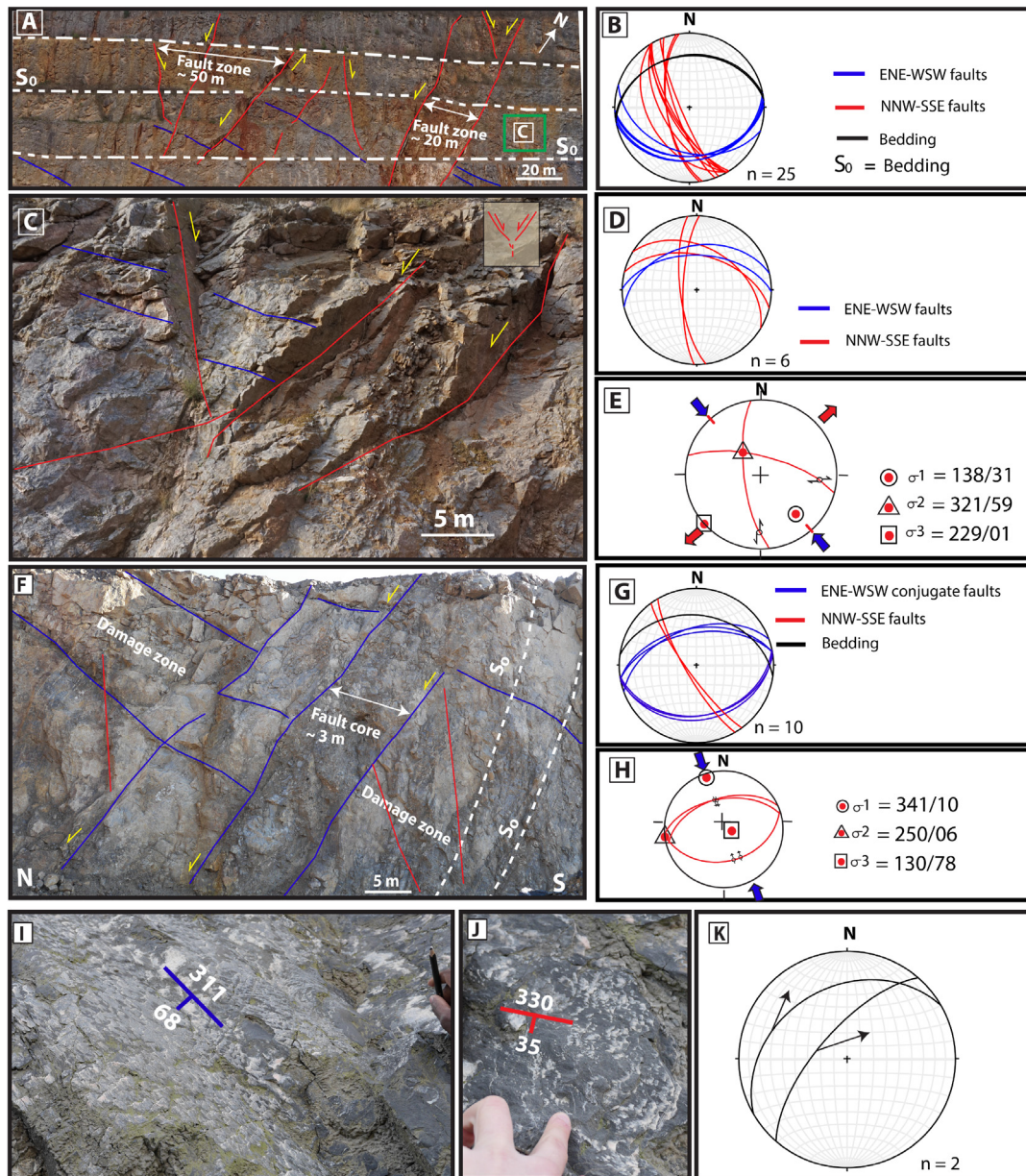


Fig. 2. Fault networks architecture in the Steltenberg quarry: (a) high-resolution 2D outcrop orthorectified photograph with NE-SW view into the quarry with two dominant fault zones i.e., high angle NNW-SSE normal faults (red) and low-angle ENE-WSW reverse faults (blue); (b) stereonet of the measured fault networks with bedding; (c) a close-up of (a), showing the conjugate normal fault where the NNW-SSE sub-horizontal σ_1 was derived; (d) and (e) stereonet and the inversion analysis of the measured conjugate normal faults with the PBT axes method; (f) photograph with E-W view of a typical ENE-WSW low-angle reverse fault with damage zone and core, which often occurs in conjugate pattern; (g) and (h) stereonet and the inversion analysis of the measured conjugate low-angle reverse faults with the P-B-T axes method; (i), (j) faults slip surfaces with an evidence of internal shear and mineral precipitation (mainly quartz and calcite); (k) stereoplot indicating sense of movement of the hanging wall block. Inversion calculations were performed with Win-Tensor software.³³

kinematic boundary conditions were applied onto the model boundaries to reproduce the effect of tectonic forces. Kinematic boundary conditions were applied in a form of pre-described displacements with an assumption of drained loading and with fault zones being represented as 2D planes of weakness with lower stiffness properties in respect to the rock mass.

To discretize the numerical solution, the high complexity of the heavily faulted and folded structures of the region and inhomogeneous rock mass properties was resolved with the finite element method (FEM). The 3D geomechanical model was described using a partial differential equation of the force equilibrium.

After an initial model was solved, numerical results had to be calibrated prior to their interpretation and application. As proven by Ref. 5, the quality of 3D geomechanical models depends not necessarily on the simulation technique but the amount and quality of calibration data. Therefore, the concept developed in this study uses a comprehensive calibration dataset, independent of input data, and validates it against the numerical results. The calibration data points were adjusted in reasonable limits until discrepancies with numerical results were minimized and a best-fit model was achieved. The input data includes basic model assumptions, model geometry, rock mass and fault zone properties, initial stress, and boundary conditions, whereas the

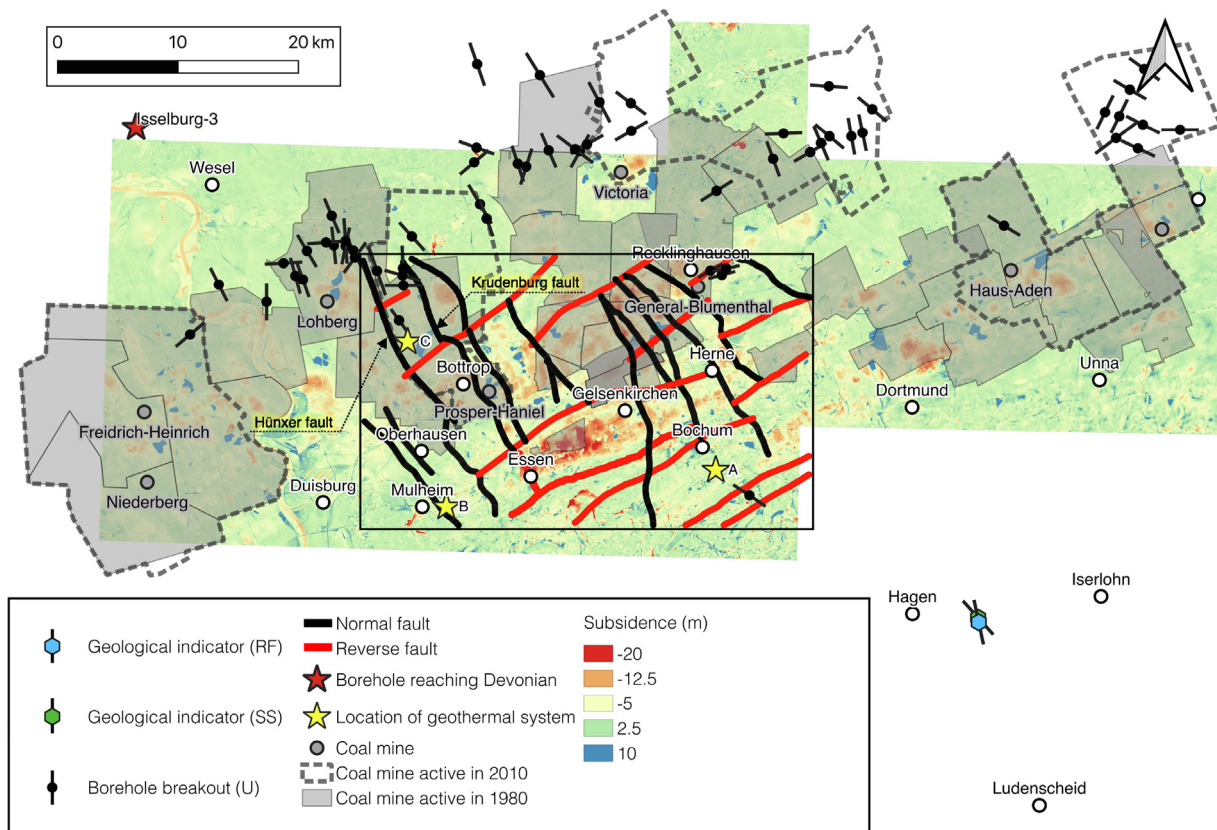


Fig. 3. The stress map of the Ruhr region with coal mines, distribution of subsidence,³⁷ and fault zones included in the numerical model (increasing length of the borehole breakout line marker indicates higher stress indicator quality); model area outlined with a black rectangle.

calibration dataset includes magnitudes of S_v , S_{Hmin} , S_{Hmax} , and θ_{SHmax} acquired from in situ measurements. This first step concerns calibrating the orientation of the applied boundary stresses by comparing θ_{SHmax} obtained from in situ measurements. In the second step, S_v magnitudes obtained from geophysical logging are calibrated against simulated S_v values. The third step assumes, calibrating magnitudes of both S_{Hmin} and S_{Hmax} acquired from in situ measurement by varying pre-described kinematic displacement conditions. As the variety of displacement boundary conditions exist for calibration of a single S_{Hmin} value, there is only one pair of displacement boundary conditions that fits both horizontal stress magnitudes.¹ The mean error, $\Delta\bar{S}$, between simulated and calibration value was computed as

$$\Delta\bar{S} = \frac{1}{l} \sum_{i=1}^l |S_i - \hat{S}_i|, \quad (2)$$

where, l is the number of data points, S_i is the calibration value and \hat{S}_i is the simulated value.

Once the numerical simulation was successfully calibrated, several scalar values, besides the direct results of the simulation, including (i) θ_{SHmax} , (ii) regime stress ratio (RSR),⁵² and fault-specific parameters such as (iii) shear, τ , and (iv) normal effective stresses, σ_n ,⁵³ (v) slip tendency, T_s ,⁵⁴ (vi) dilatation tendency, T_d ,⁵⁵ and (vii) Coulomb failure function, CFF ,⁵⁶ were computed. In addition to the model calibration with acquired in situ data, results from fault-slip analysis, distribution of subsidence,³⁷ induced seismicity (Ref. 49; Fischer, K.D. pers. comm.), and indications of fault permeability from coal mining activities^{57,58} in the Ruhr region were used to confirm the reliability of the numerical results.

4. Model setup

4.1. 3D structural-geological model

The base of any subsurface numerical modelling is a 3D structural-geological model. For this purpose, eight stratigraphic units, based on the CICM (Coal Inventory Calculation Model) model (e.g., Refs. 59, 60), were acquired from the Geological Survey of the North Rhine-Westphalia (Germany) in the MOVE software.⁶¹ The stratigraphic units are Quaternary, Cretaceous, Westphalian C1, B1, A2, and A1, Namurian CB, Namurian AB, Lower Carboniferous, and Devonian. 20 major fault zones were implemented in the 3D structural-geological model. The architecture of fault zones was extracted from geological maps, geological cross-sections, and geometries of stratigraphic units. Considering results from the deep seismic reflection and the implications from studies in Devonian quarries in the south of the Ruhr region, a continuous fault direction (i.e., NW-SE, NNW-SSE, and NE-SW) down to the bottom of the model was assumed.^{28,34,62}

For data handling purposes and computational efficiency, simplifications to the model geometry were made accepting resolution losses. This resulted in merged stratigraphic units of Quaternary, Cretaceous, and Westphalian layers called later Westphalian and geometry simplification of the stratigraphic horizons. This was due to (i) degenerating or intersecting layer elements, (ii) layer thickness being too small to accommodate effective model discretization, or (iii) layers having relatively similar mechanical properties. In addition, few of the imported fault zones were shortened, mainly at fault intersections and model boundaries, due to discretization issues and/or degenerate elements. The 3D structural-geological model and its implementation into the FEM environment is presented in Fig. 1.

Table 1

Rock mass properties of the lithostratigraphic units in the 3D geomechanical model of the Ruhr region with data from ^ARef. 27, ^BRef. 63, ^CRef. 64, ^DRef. 66, ^ERef. 34, and ^FRef. 65 (Shl: shale, Sst: sandstone, Slt: siltstone, C: coal, Lst: limestone, D: dolomite).

No	Lithostratigraphic unit	^A Composition	ρ_B (kg m ⁻³)	E_s (GPa)	ν
1	Westphalian C-A	50% Shl, 27% Sst, 26% Slt, 12% C	^{A, B} 2.459 ± 151	^{A, C} 11.7 ± 7.4	^D 0.28
2	Namurian C	42% Shl, 34% Sst, 16% Slt, 8% C	^{A, B} 2.529 ± 142	^{A, C} 15.7 ± 10.2	^D 0.28
3	Namurian B-A	36% Shl, 36% Slt, 28% Sst	^{A, B} 2.697 ± 155	^{A, C} 35.0 ± 31.5	^D 0.28
4	Lower Carboniferous	62% Shl, 33% Lst, 5% Slt	^{A, B} 2.815 ± 116	^{A, C} 68.3 ± 51.2	^E 0.33 ± 0.05
5	Devonian	45% Lst, 32% Slt, 14% Sst, 4% Shl, 3% D	^E 2.640 ± 88	^{E, F} 49.9 ± 10.2	^E 0.33 ± 0.05

4.2. Rock mass properties

Bulk density, ρ_B , static Young's modulus, E_s , and Poisson's ratio, ν , were selected to define the rock mass properties (Table 1). Static properties of the Carboniferous rock mass were derived from geophysical logging results (i.e., P-wave velocity log) from the Münsterland-1 borehole.²⁷ Gardner's relation⁶³ was applied to acquire ρ_B values of specific lithostratigraphic units. E_s values were obtained from correlation of P-wave velocity results from the Münsterland-1 borehole and destructive laboratory tests on a range of Upper Carboniferous rocks (i.e., sandstones, siltstones, and shales) from the Ruhr region.⁶⁴ Poisson's ratio values were recomputed based on the P- to S-wave ratio acquired from geophysical logging results from a middle-deep exploration borehole in the south-eastern part of the model area. For the Devonian unit, results from laboratory studies by Ref. 34 were utilized with static values recomputed from correlations by Ref. 65.

4.3. Boundary conditions and fault zone implementation

The model volume is 36.9 km × 22.4 km × 6.0 km. The model coordinate system is aligned with the mean θ_{SHmax} of the central part of the Ruhr region. To reproduce the effects of plate tectonics pre-described displacements were applied orthogonally onto the model, assuming the main tectonic compression from the Alpine Front.⁶⁷ The southern model boundary was displaced (i.e., shortened) by 66 m while the eastern and western boundaries were displaced (i.e., elongated) by 2 m each. No displacements were allowed in the direction perpendicular to the northern model boundary, however, a movement in a tangential direction of this boundary was allowed. The bottom of the model was fixed in z-direction allowing for horizontal displacements. The top of the model remained free of constraints.

For the computation of effective stress values, constant Biot's coefficient of 0.65⁶⁸ and a P_p gradient of 10.8 MPa km⁻¹, recomputed from density of mine waters sampled across the Ruhr region⁶⁹ and drilling fluid densities applied in boreholes,⁵⁶ analysed in this study (Fig. 4), were assumed.

Fault zones control the mechanical and fluid-flow properties of the Earth's upper crust (e.g., Refs. 70–72). There, semi-brittle shear zones or pre-existing or early formed brittle structures locally perturb the stress state and dominate the process of fault development.^{73–75} As fault zones grow, progressive shearing and interaction of the inherited structures control slip zones and slip surfaces, which are accommodated in the fault cores and damage zones, and, in return, affect the near-fault host rock properties and generate stress perturbations.^{76–79} In 3D geomechanical modelling, the term fault zone is often used to refer to a 2D plane along which concentration of deformation with a known shear sense of movement. Fault zones were incorporated into the model volume as distinct 2D planes of weakness with specific stiffness properties. This was performed by deeming fault zones as thin elastic layers, which is a common assumption in modelling of thin or high aspect-ratio structures sandwiched between other relatively low aspect-ratio structures in FEM environments, and a common consideration in many geomechanical modelling studies (e.g., Refs. 3, 80–84). On interior boundaries, a thin elastic

layer decouples displacements between the two sides of the boundary. The two sides are then connected by elastic forces with equal size but opposite directions, proportional to the relative displacements and velocities

$$\sigma' \cdot \vec{n} = \vec{k}_A \cdot \vec{u}, \quad (3)$$

where σ' is the effective stress tensor, \vec{n} is a normal vector of the boundary of the model, \vec{k}_A is the spring constant in a normal and tangential direction, and \vec{u} is the displacement vector composed of the displacement on each side of the fault zone.

Studies by Ref. 85 on fractured Opalinus Clay formations indicated that Young's modulus of a fault zone can vary by several orders of magnitude between fault core and host rock and can approach values as low as 0.1 GPa for clay-filled faults. The fault-specific properties cannot be measured and are rarely investigated under laboratory conditions. As a consequence, there is a lack of fault-specific properties to populate 3D geomechanical models. The fault-specific properties will also change from fault to fault and along a trace of one particular fault. In the light of the above arguments, fault stiffness properties, estimated from an assumption of constant fault thickness and elastic properties of a clay gouge, were assumed constant across the model and amounted to a normal stiffness of 0.17 MPa mm⁻¹, and shear stiffness of 0.06 MPa mm⁻¹. For an assessment of fault reactivation risk, all faults were deemed cohesionless. The coefficient of sliding friction, μ , ranging between 0.5, as a lower bound, and 0.7, as an upper bound, was assumed for the Carboniferous layers.^{4,86–89} For Devonian layer μ between 0.6, as a lower bound, and 0.8, as an upper bound^{90,91} was assumed.

4.4. Model discretization and calibration

The numerical model volume was discretized with a minimum and maximum element size of 130 and 800 m, respectively. Tetrahedron elements were selected due to their flexibility to describe complex 3D geometries. The model is discretized into 1.7 million tetrahedral elements. The average element quality amounts to 0.65, where 0.0 represents a degenerated element and 1.0 represents a completely symmetric element. Fault zones were discretized by 81000 triangles with an average element quality of 0.87.

The calibration of θ_{SHmax} was performed with four borehole breakout measurements from Ref. 46, five borehole breakout measurements from this study, and one measurement from hydrofracturing measurements.⁴⁴ Collected θ_{SHmax} measurements represent stress indicator quality between C and E⁴⁷ (Fig. 4). The A to C stress indicator quality measurements only amounted to $\Delta\theta_{Hmax}$ of 6.2 ± 7.0°. As discussed before, few θ_{SHmax} measurements, located in the modelled area, are oriented perpendicular to the regional θ_{SHmax} .⁴⁸ These measurements were deemed to be misinterpretations of analysed borehole breakouts and, by rotating them 90°, were added to the calibration dataset. The overall $\Delta\theta_{Hmax}$, based on A to E stress indicator quality measurements, amounted to 16.2 ± 16.5°. For the calibration of S_v magnitude, results of rock bulk density from geophysical logging in ten boreholes with depths between 0.4 to 1.8 km within the

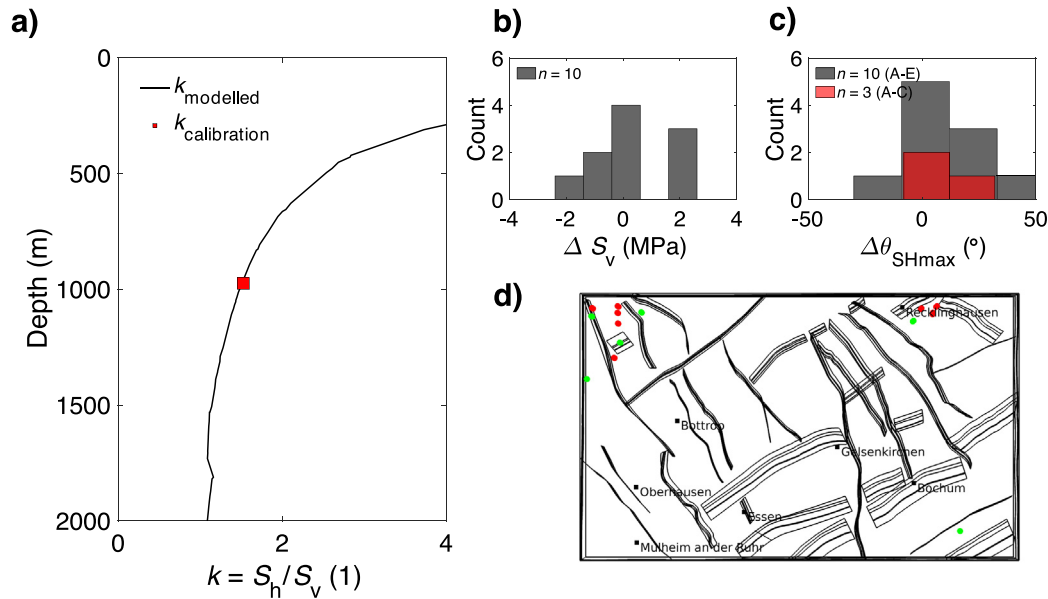


Fig. 4. Calibration of the numerical model: (a) calibration of S_{hmin} and S_{Hmax} magnitudes represented with k -value; (b) calibration of S_v magnitude; (c) calibration of θ_{SHmax} ; (d) location of calibration points within the model box (some of the locations included measurements of both S_v magnitude, marked red, and θ_{SHmax} , marked green).

Carboniferous layers were utilized (Fig. 4). The match between calibration and modelled values amounted to ΔS_v 1.04 ± 0.8 MPa. One pair of S_{hmin} and S_{Hmax} measurement was available within the model volume.⁴⁴ This hydrofracturing measurement was performed at depth of 975 m in the area of the former General Blumenthal mine. The measurement indicated a strike-slip stress regime with $S_{hmin} < S_v < S_{Hmax}$ and k -value of 1.53. Overall, a satisfactory agreement between modelled and calibration data for measurement was achieved (Fig. 4).

5. Results

5.1. 3D in situ Stress Tensor

Results of the calibrated 3D geomechanical model are presented in Figs. 5 and 6. The regime stress ratio (RSR) varies depending on the lithostratigraphic units horizontally and laterally (Fig. 6). A strike-slip to transpressive regime dominates at the surface, predominantly in the Westphalian layer (1.51 ± 0.45), and changes with depth to a more transtensional regime (Namurian C, B and Devonian layers with RSR of 1.13 ± 0.22 , 1.12 ± 0.18 , and 1.27 ± 0.40 , respectively), that prevails at greater depths. Local changes from transtension to transpression were observed mainly in the Lower Carboniferous layer with RSR of 1.90 ± 0.32 . The modelled RSR values do not exceed, on average, 2.2. Furthermore, an increase of RSR value in the vicinity of fault zones is observed.

Higher S_{Hmax}/S_{hmin} ratios and differential stresses are observed at greater depths in comparison with the upper-most Westphalian and Namurian layers, as well as for the central (i.e., the vicinity of Bottrop and Oberhausen) and north-western (i.e., area of the Prosper-Haniel mine) parts of the model where the Devonian units are deeper than in the southern sections. Such a pattern highlights a potential trend of increased differential stress towards the north-western Ruhr region. Areas with lowest differential stresses and S_{Hmax}/S_{hmin} ratios are observed in the south-east of the model area, close to the city of Bochum. Higher

differential stress concentration is visible in the proximity of fault zones, especially around their curves and tips. This proves that the state of stress could be dominated by the fault architecture and is an important observation for the interpretation of fault-adjacent in situ stress measurements in a more regional context. A generalization can be made, that synclines represent areas of increased differential stresses, whereas anticlines present the opposite, which has been extensively observed and discussed in the literature (e.g., Refs. 92, 93). θ_{SHmax} in the modelled area ranges between NW-SE and NNE-SSW direction. In the vicinity of NW-SE striking fault zones θ_{SHmax} reorients counterclockwise (from the N-S direction) and in the vicinity of NE-SW fault zones, it reorients clockwise (from the N-S direction). The rotation of θ_{SHmax} with depth is observed especially in the vicinity of faults and along anticlines (clockwise) and synclines (counterclockwise). Similar phenomena have been observed in the literature (e.g., Ref. 94).

As an example, in Fig. 5 (a), (d), and (g) numerical results of in situ stress state for the reservoir depth of 5 km were presented. Based on these figures, it can be observed that the S_{Hmax}/S_{hmin} ratio at this depth varies between approximately 1.7 and 2.1. The differential stresses at 5 km depth vary on average between 80 and 130 MPa, with some localized increases up to 180 MPa. θ_{SHmax} at 5 km depth is relatively homogeneous and varies between 170 and 180°.

5.2. Fault-specific parameters

Comparison of the reactivation potential pattern in 3D with the frictional resistance of a fault zone can provide a useful constraint on the probability of its reactivation. Faults or fault segments, where the calculated ratio of shear to effective normal stress overcomes the frictional resistance are considered as potential locations of reactivation. The high dependence of T_s , T_d and CFR on the fault architecture and prevailing in situ stress state is displayed in Fig. 6, where colder colours present lower values and hotter colours presenting the opposite.

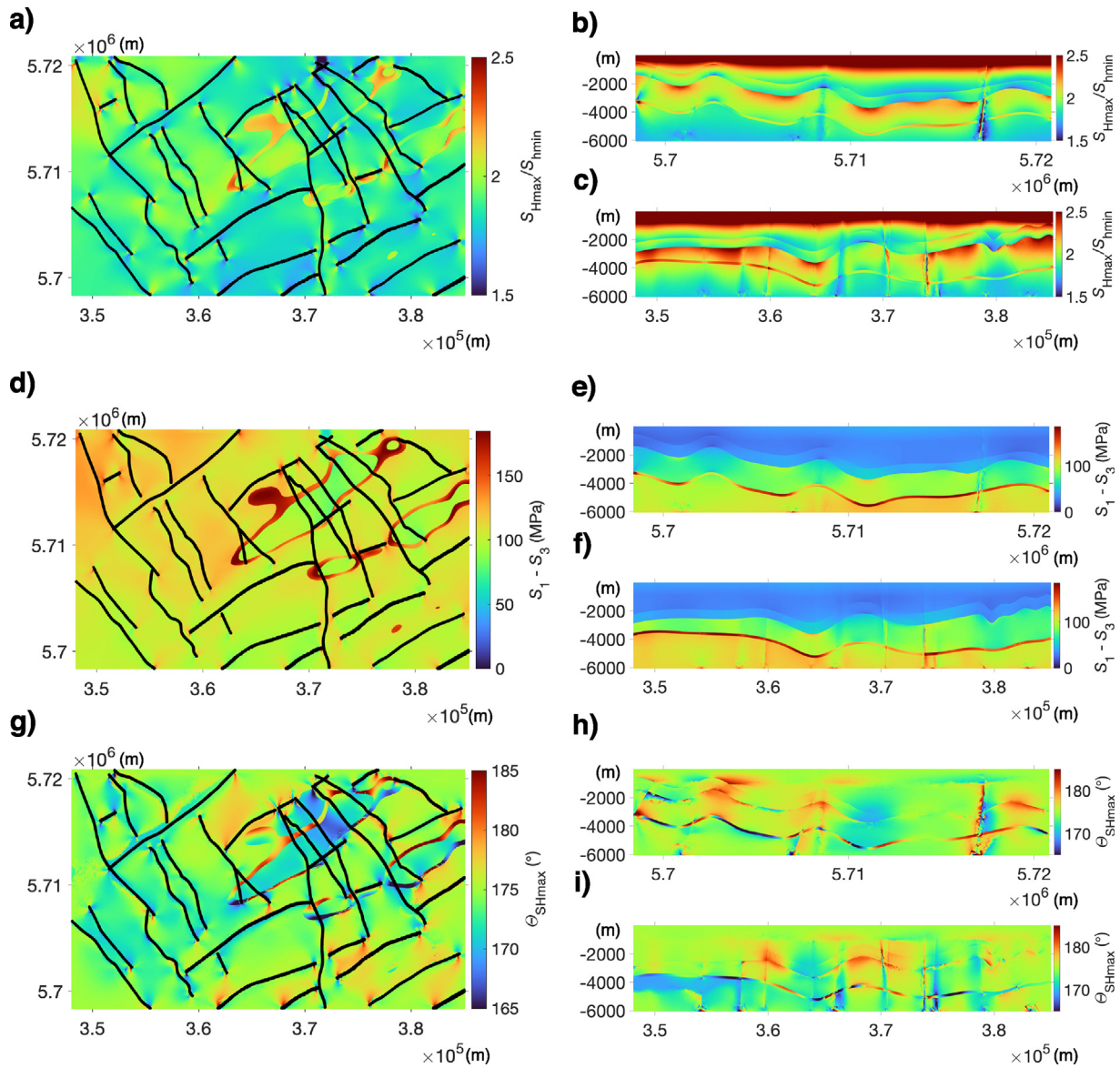


Fig. 5. Results of the numerical model with fault zones marked with solid black lines: (a) S_{Hmax}/S_{Hmin} ratio at 5000 m depth; (b) S_{Hmax}/S_{Hmin} ratio across the N-S cross section; (c) S_{Hmax}/S_{Hmin} ratio across the W-E cross section; (d) differential stress at 5000 m depth, (e) differential stress across the N-S cross section; (f) differential stresses across the W-E cross section; (g) θ_{SHmax} at 5000 m depth; (h) θ_{SHmax} across the N-S cross section; (i) θ_{SHmax} across the W-E cross section.

It would be incorrect to expect that one value of μ will accurately represent frictional properties of all faults confined within the numerical model of such a great extent. The methodology applied in this study compares numerical results against a range of possible frictional coefficients, expected in a given lithostratigraphic unit. For a case of T_s being higher than the upper limit on the slip threshold, that particular fault zone can be considered as reactivation prone. Statistical distribution of T_s , T_d , and CFF grouped into NW-SE to NNW-SSE (left) and NE-SW (right) striking fault zones is presented in Fig. 7. One can observe that the great majority of the NW-SE to NNW-SSE striking fault zones can be considered as being close to the critical state (with T_s median of 0.40) and open (with T_d median of 0.67) in the prevailing in situ stress configuration (Fig. 7). The NE-SW striking faults, on the other hand, could be considered as “locked” under prevailing in situ stress state and impermeable (with T_s median of 0.32 and T_d median of 0.31). Based on the lower limit of μ (i.e., 0.5–0.6) around 16% of all NW-SE to NNW-SSE striking fault segments can

be considered active (i.e., with $CFF \geq 0$), in comparison to 5% for the NE-SW striking fault segments. Assuming an upper limit on μ (i.e., 0.7–0.8), 2% of all NW-SE to NNW-SSE and only 0.2% of NE-SW striking fault segments can be considered as active.

6. Discussion

6.1. Stress rotation

A few “unexpected” θ_{SHmax} re-orientations, striking approximately 90° from the regional θ_{SHmax} , were observed from borehole breakout analysis within the modelled area. These θ_{SHmax} rotations, which by adding 90° were eventually added to the calibration dataset, could not be explained with the results of this model. It is, thus, expected that such θ_{SHmax} re-orientations could be related to either (i) wrongly reported reading from the caliper tool, (ii) mistakenly picked borehole breakouts (i.e., extended drilling-induced tensile fractures in weak layers, collapsed

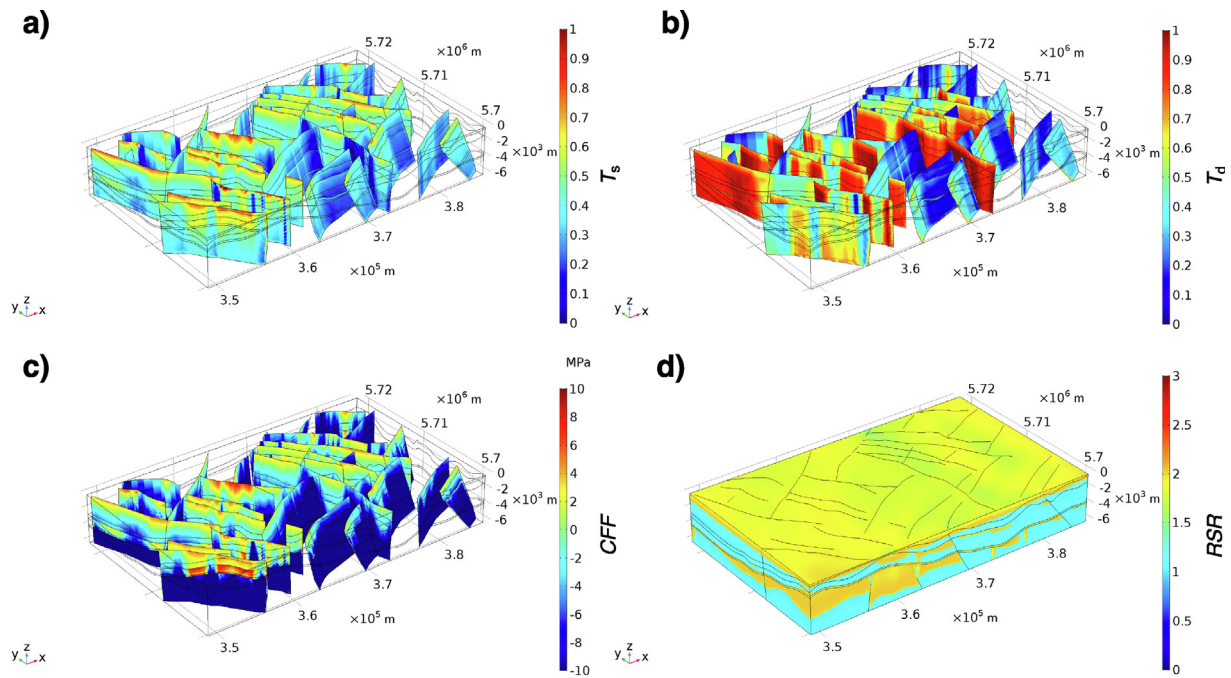


Fig. 6. Results of the numerical model: (a) slip potential, T_s ; (b) dilatation potential, T_d ; (c) Coulomb failure function CFF ; (d) regime stress ratio RSR .

preexisting open fractures or filter cake along caved zones picked instead of borehole breakouts), or (iii) a near-isotropic horizontal stress state which would cause significant rotations of stress due to small local stress sources.^{6,95} As the latter hypothesis based on the available in situ stress data from the region (i.e., Refs. 38–44) and being supported by the results from the numerical model presented in this study, can be excluded only (i) and (ii) are to be expected as potential reasons for 90° rotation of θ_{SHmax} .

6.2. Model reliability

Uncertainties introduced by the input data constitute of (i) basic model assumptions, (ii) rock mass and (iii) fault zone properties, (iv) the geometry of fault zones and lithostratigraphic horizons, (v) initial stress, and (vi) boundary conditions. The developed model suffers from simplifications, which may pose limitations to its applicability. This can be attributed to the fact that the majority of used data, being it input or validation, comes exclusively from the Upper Carboniferous strata, which was of primary interest to the coal mining industry in the region. Deeper formations were, until now, of no interest and, as a result, no data is available from these layers. The model reliability can be, thus, considered much higher in Upper Carboniferous units than in the Lower Carboniferous and Devonian units.

One of the core model unknowns remains the uncertainty of the existence of Devonian layers underlying the Carboniferous strata across the Ruhr region. The only indication of such comes from interpretations of the DEKORP 2-N seismic line.^{28,62,96} Besides, fault zone geometry at greater depths remains uncertain. Except for a few seismic events in the north-western part of the model area located below 3 km aligning with the fault surface traces⁴⁹ and an outcrop study by Ref. 34, which proved similar orientation of discontinuities in the Devonian and Carboniferous units, there are no clear proof of the fault zones existence below Carboniferous layers. The presence and architecture of implemented fault zones may, in reality, differ from the ones constructed in the model, which is especially the case for the deeper subsurface. The assumptions made in this study shall be

validated with 3D seismic surveys and results from deep exploration drilling campaigns in the region. Additionally, shortening of the fault zones at fault intersections, as carried out in this study, could have a significant effect on the state of stress. The quantification of this effect was limited by the FEM software in use and should be investigated in future studies.

Simplifications to the model geometry were performed primarily for maintaining model practicability and for accommodating limitations of the FEM software. Implemented formation horizons represent lithostratigraphic units and not specific rock types, which is due to the highly complex geology of the Carboniferous units composed of cyclothem. These highly complex stratigraphic sequences pose significant challenges during discretization, solving, and population of the numerical model with properties. As a consequence, to analyse the in situ stress state in a more regional context, some degree of homogenization of rock strata based on e.g., stiffness contrasts, as performed in this study, will always have to be applied in the Ruhr region.

An assumption of constant Poisson's ratio for the Upper Carboniferous layers, based on geophysical logging results, should be considered as a big simplification of the subsurface conditions. In reality, elastic properties of the Upper Carboniferous layers will vary significantly, due to the strong interbedding of rocks with much different elastic properties (i.e., cyclothem). Additionally, an assumption of constant Biot's coefficient throughout the whole model should be also considered as a big simplification. For the mitigation of uncertainties in the future geomechanical modelling efforts, it is advised to prioritize the above-mentioned properties, desirably in reservoir-specific conditions.

More than 700 years of hard coal extraction superimposed a significantly different secondary stress field in the Ruhr region. This is due to e.g., S_v decrease from a significant amount of rock withdrawal, P_p fluctuations due to mine water pumping, or slip on preexisting and/or newly created faults and/or fractures. The influence of coal mining is difficult to assess. This is mainly due to the vast extend the mining industry was present in the region and the requirement of detailed information on the location of the subsurface infrastructure and its current state (i.e., if mine is left empty, flooded, or cemented). This goes much beyond the scope of this study.

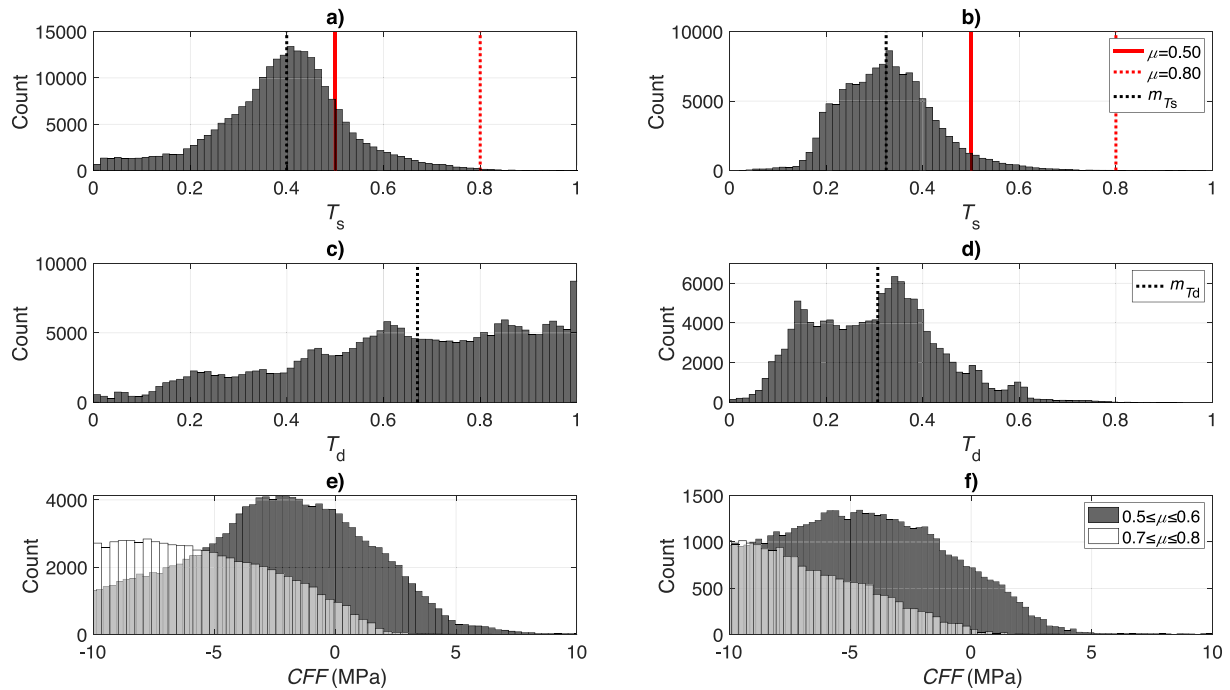


Fig. 7. The reactivation potential of modelled fault zones: (a) slip potential, T_s , of the NW-SE to NNW-SSE oriented fault zones (T_s median, m_{T_s} , equals to 0.40); (b) T_s of the NE-SW oriented fault zones (m_{T_s} equals to 0.32); (c) dilatation potential, T_d , of the NW-SE to NNW-SSE oriented fault zones (T_d median, m_{T_d} , equals to 0.67); (d) T_d of the NE-SW oriented fault zones (m_{T_d} equals to 0.31); (e) Coulomb failure function, CFF , of the NW-SE to NNW-SSE oriented fault zones; (f) CFF of the NE-SW oriented fault zones.

Due to the ongoing mine water pumping activities in the Ruhr region, water table levels in the subsurface have been significantly reduced. Currently average water table level in coal mines amounts to approximately 600 m,^{97,98} where in some cases water level reduced to 1.2 km were observed (www.bid.rag.de). Such significant differences in mine water table levels will cause pore pressure changes and result in a decrease in reactivation potential of major fault zones. As a consequence, the effect of P_p changes on the in situ stress state in the Ruhr region cannot be regarded as marginal and shall be investigated prior to the development of a deep geothermal system therein. This is especially true for locations in the vicinity of the former coal mines or mine water pumping stations. It remains, also, not clear if or to what extent stress magnitudes used for the model calibration were affected by coal mining activities.

It shall be emphasized, that the assumption of a homogeneous fluid pressure gradient should be considered a significant simplification of the pore pressure field in the study area. In large and faulted domains like the one represented in our model, significant fluid pressure differences (due to the influence of e.g., topography, fault zones, and/or rock mass heterogeneities) are expected. Such differences will undoubtedly affect the stability of the fault planes and, therefore, provide different results from the ones presented with our model. The simplified approach used in our study can be reasoned by the lack of reliable hydraulic properties of the rock layers and fault zones at depth which would introduce a set of uncertainties as well as a relatively minor influence of topography. As a result, a homogeneous pore pressure field, although being apriori incorrect, in our case is the best approximation.

6.3. Uncertainty quantification

To be able to quantify the reliability of the numerical model, a method developed in Ref. 5 was applied. Using this approach, the

mean T_s value for all modelled fault zones, for which variability was introduced by the uncertainties of the rock mass, fault zone properties, and calibration data, was recomputed. For the sake of simplicity, the basic model assumptions, boundary conditions, model geometry (i.e., the architecture of horizons and faults), and initial stress conditions were deemed as invariable. T_s was computed for several model scenarios in which the extreme values of the range of uncertainties of the input and calibration parameters were used. This allowed deriving the individual impact of specific model parameters and quantify ones that are the most crucial. The results of T_s for each model scenario were subsequently compared to the mean T_s from the best-fit model. Across the Ruhr region, fault zones will have much different stiffness properties depending on their filling type, which can range from carbonate material (e.g., calcite), being much stiffer than the host rock, to sulfides or clay minerals, being significantly more elastic.^{34,99} To represent the most extreme case of fault filling material stiffness in the Ruhr region, a case of a fault filled with carbonate material with a normal and tangential stiffness of 7.39 MPa mm⁻¹ and 1.88 MPa mm⁻¹, respectively, were assumed. As proven by Refs. 1, 100, 101, uncertainties related to the model calibration with multiple available S_{hmin} and S_{hmax} pairs may be significant. Unfortunately, due to only one pair of horizontal stresses with the detailed location being available within the modelled area, uncertainties related to the model calibration could not be properly assessed. To showcase the impact of the calibration process on the model results, the S_{hmax} magnitude (property ever-burdened with a high uncertainty)¹⁶ was recalculated based on the frictional faulting theory⁵³ assuming a strike-slip faulting regime, S_{hmin} magnitude from Ref. 44 and an upper bound on μ of 0.7 for Upper Carboniferous units.^{4,86-88} Computations with these assumptions amounted to a k -value and S_{hmax} values of 57.3 MPa and 1.68, respectively. The calibration of the numerical model was then initiated with the new data

and T_s uncertainty evaluated. The variations introduced by the independent model parameters were added together and led to a combined T_s variability of ± 0.1 with the main source of variability resulting from the rock mass properties.

6.4. Model validation

6.4.1. Validation against fault-slip data

Two similar striation sets were observed on analysed fault surfaces in the Steltenberg quarry (Fig. 2i, j, k). One of them displays a horizontal component of the movement in the same direction as that of the fault zone's hanging wall, having an approximate NNW-SSE orientation. Conversely, the second set of striae lacks a visible sense of movement but generally trends N-S to NE-SW. The NE-SW direction of the fault movement, as presented in Fig. 2k, agrees with the direction of fault movement computed from the model results, which proves its reliability. To reconstruct the stress field that has affected Devonian carbonates, paleostress regimes from the generated stress tensors from the Steltenberg quarry (Fig. 2d, e, g, h) were analysed using the stress ratio, ϕ , and, following the stress index, R' .³³ All over the study area, results consistently indicate both reverse and strike-slip faulting regimes. For the reverse faulting regime, the ENE-WSW thrust faults show sub-horizontal NNW-SSE oriented σ_1 (Fig. 2g, h) and having an R' value of 2.5, which is associated with pure compression. In contrast, the NNW-SSE striking normal conjugate faults indicate a strike-slip regime with the R' of 1.5 and an approximately NW-SE sub-horizontal σ_1 (Fig. 2d, e). From the kinematic analysis in places within the quarry, it was determined that more than one stress state has successively occurred due to varied principal stress axis directions. Although located around 12 km away from the model area, results of the fault-slip analysis in the Steltenberg quarry agree with the simulated RSR values.

6.4.2. Validation against subsidence data

The distribution of subsidence in the Ruhr region³⁷ was used to validate numerical results based on visual comparison. By comparing the modelled RSR values at depths below the coal mining levels (i.e., 1.9 km), a good correlation between subsidence and extensional areas ($RSR < 1$) was observed. This phenomenon confirms the correlation between stress regime and vertical motion of the rock mass. Plateaued regions correlate with more compressional areas ($RSR > 1$), which was observed in the southern parts of the model. Furthermore, major NW-SE striking faults confine the amount of subsidence³⁷ potentially proving their recent activity in the prevailing in situ stress state (Fig. 3). It can be, thus, stated that the results of the numerical model are in agreement with the distribution of subsidence in the Ruhr region.

6.4.3. Validation against microseismic data

More than 5100 seismic events were recorded between 2014 and 2018 at the location of the former, but at that time active, Prosper-Haniel coal mine in the north-western part of the model⁴⁹ (Fig. 3). The majority of seismic events were located at depths of active coal mining and are expected to be directly related to coal mining activities.⁵⁰ Around 140 seismic events with $M_L > 1.5$, were located at depths greater than the maximum mining depth in the Prosper-Haniel mine between 2014 and 2018 with the deepest seismic event being located at approximately 9 km (following the trace of the NW-SE striking Hünxer fault). These events, responding to the stress changes on the scale of an entire mine, could have been related to the tectonic response, resulting from coal mining, and possible reactivation of preexisting faults.¹⁰² Such occurrences were observed in e.g., the Saar coal district¹⁰³ in SW Germany. Conclusions by Ref. 104 based on a

detailed study on the correlation between specific longwall mining faces and seismic events recorded between 2016 and 2018 within the Prosper-Haniel mine, also point in this direction. They proved that some of the analysed seismic events with $M_L > 2.5$ were located at a distance of 2 to 5 km from specific longwalls and have relatively uniform waveforms with a frequency in the range between 5 and 8 Hz. Additionally, recomputed stress drops from these events were significantly higher than those assigned to the specific longwalls. These phenomena prove that the analysed events were a mixture of the ones related to the reactivation of preexisting faults (i.e., frictional earthquakes) and directly mining associated fractures.

To investigate, if seismic events below the active mining depths in the Prosper-Haniel mine were related to the fault reactivation, acquired seismic events with $M_L > 1.5$ were projected onto the model volume. 15 seismic events with $M_L > 1.5$ (with 3 events with M_L between 2.7 and 2.9) were located either directly on or in close proximity to the major NW-striking Hünxer and Krudenburg faults. These events correlate with the fault segments with high T_s and CFF values computed based on the numerical results from the 3D geomechanical model, indicating their high reactivation potential (Fig. 8). Such observation could prove that the stress changes related to the mining operations induced movement on the major NW-SE striking fault zones in that area and resulted in induced seismicity. Taking into account the error connected to the seismic event location and simplification of model geometry, the match between sections with high reactivation potential and seismic events is more than satisfactory.

To look at the seismicity within the Prosper-Haniel coal mine in greater detail, registered seismic events at depths were compared to CFF and its x , y , and z derivatives from two major fault zones (i.e., NW-striking Hünxer and Krudenburg faults) confined within the coal mine. It was observed that the majority of seismic events were confined within the Upper Carboniferous layers. As discussed before, one could deem events recorded up to ~ 2.0 km depth as being directly related to the rock excavation processes (i.e., rockfall) due to their proximity to the active coal mining depths. Events located > 2.0 km depth, could have been, instead, related to the significant stress change transfer caused by coal mining, which leads to the reactivation of preexisting faults. It is noticed that the stress release is much lower in the Devonian layer than in the Carboniferous layers, where the transition between these units, at the depth of ~ 4.2 km, correlates with a significant CFF decrease. This could potentially indicate a transition between Carboniferous and Devonian rock mass and, simultaneously, prove the accuracy of the model geometry.

Based on the observations above, it can be stated that the modelled in situ stress state in combination with assumed friction criteria is in agreement with the observed induced seismicity in the region and could potentially predict the boundary between Carboniferous and Devonian units. Even with the potentially high uncertainties of input and calibration data, and simplification of model geometry and rock mass properties, much beneficial information have been obtained. This should also suggest the high importance of further research directed towards the quantification of uncertainty sources, especially to the ones introduced by the variability of the model input parameters.

6.4.4. Validation against mining observations

It is widely assumed, that critically stressed fractures and faults are the main fluid pathways in the subsurface (e.g., Refs. 70–72). An indication of fault permeability in the Ruhr region arises from a study by Ref. 57 on the NW-SE striking Krudenburg fault located within the Prosper-Haniel mine (Fig. 3). Two major water inflows with volumes between 0.3 and $18 \text{ m}^3 \text{ h}^{-1}$

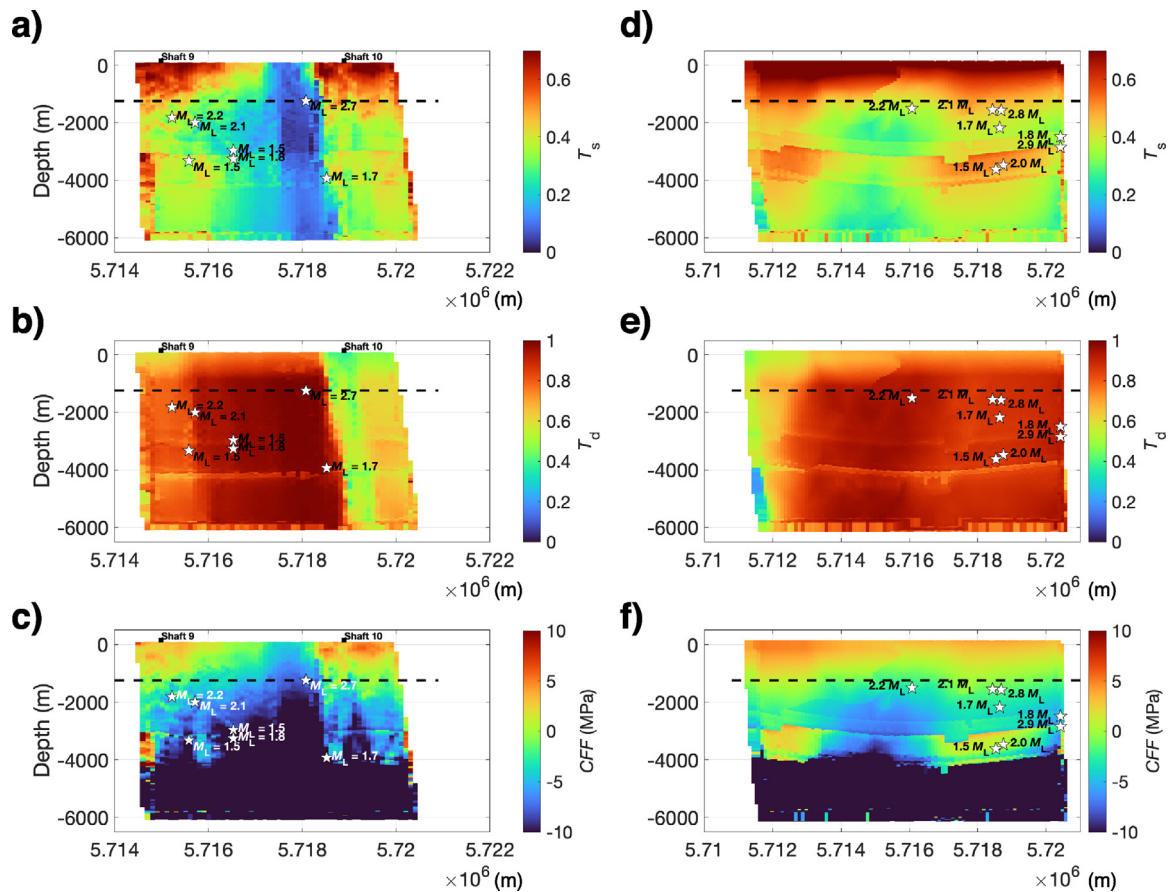


Fig. 8. Results of the numerical model for the Krudenburg and Hünxer faults (location in Fig. 3) constrained within the Prosper-Haniel mine with registered microseismic events with maximum mining depth marked with black dashed line: (a) slip potential, T_s , of the Krudenburg fault; (b) dilatation potential, T_d , of the Krudenburg fault; (c) Coulomb failure function, CFF , of the Krudenburg fault; (d) T_s of the Hünxer fault; (e) T_d of the Hünxer fault; (f) CFF of the Hünxer fault.

were observed during fault penetration between mine shaft number 9 and 10 causing major disruptions during mining operations. A successful attempt of sealing the highly permeable fault was made by removing $> 75\,000\text{ m}^3$ of water using 2.5 km of relief boreholes and injecting 5500 m^3 of grout. Based on results from the numerical model for the Krudenburg fault, the mean T_d and T_s values amount to 0.80 and 0.33, respectively. Increased T_s values are especially visible in southern and northern fault segments (Fig. 8). This agrees with the field observations by Ref. 57. Surface methane emissions studies by Ref. 58 prove that the majority of the emitted gas at the surface, in the vicinity of the city of Bochum, was emitted alongside an NNW-SSE direction. Both studies confirm the high stress criticality of the NW-SE to NNW-SSE oriented discontinuities, the stress-dependent direction of permeability within the Ruhr region, and a good agreement with the results of the numerical model.

6.5. Application for geothermal reservoirs

As an example, three different locations within the modelled area were analysed in terms of the best conditions for establishing a deep geothermal system in the Ruhr region (location in Fig. 3). From the three preselected locations, location B is deemed to be the best suited for the establishment of a geothermal system. This is due to the potential for propagating horizontal and/or subhorizontal fractures as a result of transpressive stress regime prevailing up to a depths of approximately 4.0 km, which is favourable in terms of reservoir permeability (Fig. 9). Additionally, Devonian layers, of improved hydraulic properties, are at a shallower depth in location B than in the two others. In the

location A and C, the transpressive stress regime is limited to a depth of around 1.0 km with a strike-slip regime below. The planned wellbore could be drilled towards the NE-SW direction for achieving higher productivity outputs. Once drilling in the NE-SW direction will be connected to the penetration of one of the major NW-SE or NNW-SSE striking fault zones, their reactivation could be considered as relatively likely.

7. Conclusions

In this study, a 3D in situ stress state quantification in the Ruhr region using numerical modelling was presented. The developed 3D static geomechanical model was validated against a comprehensive calibration dataset including results from geophysical logging, borehole deformation and fault-slip analysis, in situ measurements, distribution of subsidence, seismicity, and observations from coal mining operations. Spatially continuous 3D in situ stress state, as presented in this study, instead of point-wise stress information, provide an effective tool for planning subsurface operations in areas where no stress information is available. The wide range of model uncertainties could be mitigated by (i) detailed GPS measurements for constraining the amount of horizontal motion of tectonic plates, (ii) laboratory measurements of rock mass properties under reservoir-specific conditions, (iii) 2D and 3D seismic surveys, (iv) deep exploratory drilling campaigns for improved constraints on the subsurface geometry, rock mass, and fault zone properties, and (v) in situ stress measurements at greater depths and, especially, in the southern parts of the Ruhr region. Nonetheless, as for the current state of knowledge and data availability, our approach provides

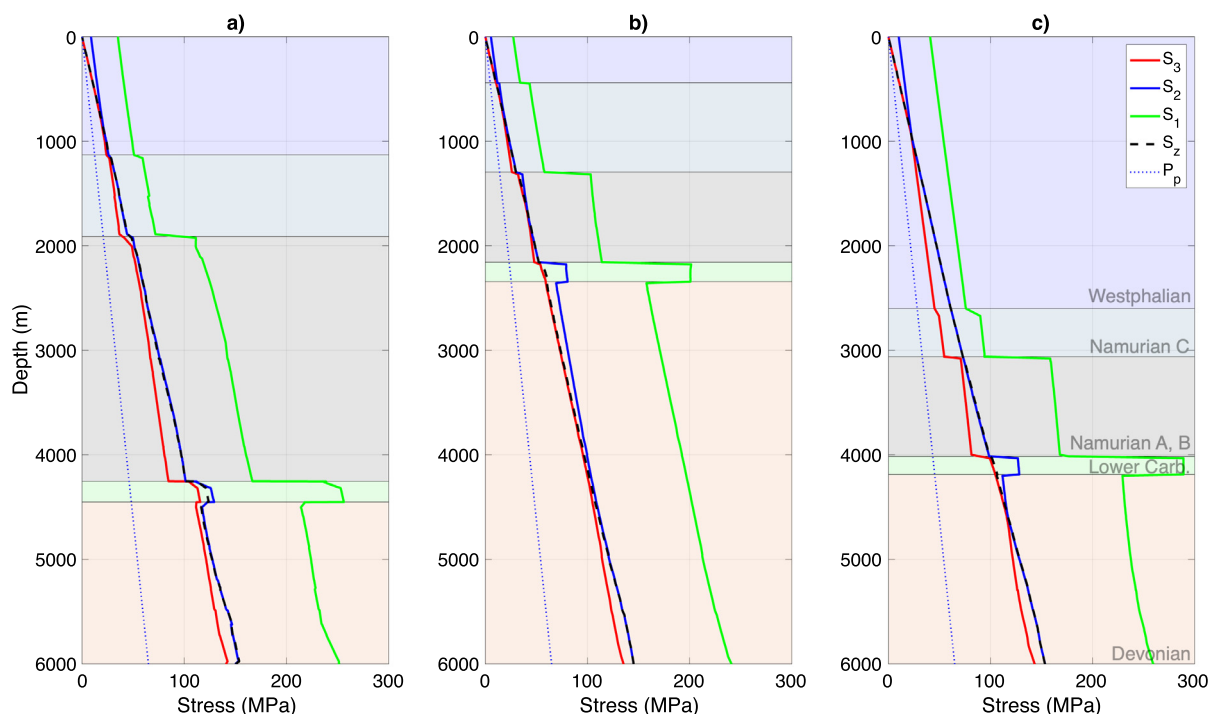


Fig. 9. Principal stresses and pore pressures for three proposed locations for an establishment of a deep geothermal system within the Ruhr region: (a) in the vicinity of the city of Bochum; (b) in the vicinity of city of Müllheim; (c) in the vicinity of city of Bottrop (detailed locations marked with yellow stars in Fig. 3).

the best estimate of the state of prevailing in situ stress tensor for applications in e.g., Thermo-Hydro-Mechanical simulations.

Funding

This work was carried out in the framework of the 3DRuhrMarie (“FHprofUnt2016”) project, which received funding from the German Federal Ministry of Education and Research (BMBF) and geomecon GmbH.

CRediT authorship contribution statement

Michał Kruszewski: Conceptualization, Methodology, Software, Validation, Formal analysis, Investigation, Data curation, Writing – original draft, Visualization. **Giordano Montegrossi:** Conceptualization, Formal analysis, Investigation, Writing – review & editing. **Martin Balcewicz:** Software, Data curation, Writing – review & editing, Visualization. **Gabriela de Los Angeles Gonzalez de Lucio:** Methodology, Software, Investigation. **Onyedika Anthony Igbokwe:** Investigation, Writing – review & editing, Visualization. **Tobias Backers:** Writing – review & editing, Supervision, Funding acquisition. **Erik H. Saenger:** Resources, Writing – review & editing, Supervision, Project administration, Funding acquisition.

Declaration of competing interest

The authors declare that they have no known competing financial interests or personal relationships that could have appeared to influence the work reported in this paper.

Data availability

The results of the three-dimensional geomechanical-numerical model including in situ stress state and fault-specific properties are available under dx.doi.org/10.24406/for-datis/205.105

Acknowledgements

The authors would like to thank Geologischer Dienst Nordrhein-Westfalen and RAG Aktiengesellschaft for data provision. The authors thank also geomecon GmbH for support during the preparation period of this manuscript. Additional thanks go to Dr. Kasper D. Fischer from Seismological Observatory at Ruhr-University Bochum for providing seismic data. The authors would also like to thank Prof. Dr. Stefan Harnischmacher from the University of Marburg for providing subsidence data from the Ruhr region, Mr. Ulf Grimhardt from RAG Aktiengesellschaft for providing coal mine maps, Prof. Dr. Oliver Heidbach from German Research Centre for Geosciences for constructive discussions about the stress field of the Ruhr region, and Mr. Mohamed Ibrahim Moursy from RWTH Aachen University for digitalization of geophysical data. The authors also thank Dr. Benedikt Ahrens from Fraunhofer Research Institution for Energy Infrastructures and Geothermal Systems IEG and Dr. Mandy Duda from Ruhr University Bochum for support during the preparation of this manuscript. The authors would like to express their deep appreciation to Mr. Gerd Klee from Solexperts GmbH for sharing in situ stress data from the Ruhr Carboniferous.

Liability disclaimer

The authors reserve the right not to be responsible for the topicality, correctness, completeness, and quality of the information provided. Liability claims regarding damage caused by the use of any information provided will be rejected. Conclusions made in this study are solely opinions of the authors and do not express the views of the employer, university, or funding agency.

References

- Ziegler M, Heidbach O. The 3D stress state from geomechanical-numerical modelling and its uncertainties: a case study in the Bavarian Molasse basin. *Geotherm Energy*. 2020;8.

2. Parisio F, Vilarrasa V, Wang W, Kolditz O, Nagel T. The risks of long-term re-injection in supercritical geothermal systems. *Nature Commun.* 2019;10.
3. Meier T, Backers T. Reactivation of fault zones due to thermo-poroelastic stress changes. 2018.
4. Hunfeld LB, Niemeijer AR, Spiers CJ. Frictional properties of simulated fault gouges from the seismogenic groningen gas field under in Situ P-T-chemical conditions. *J Geophys Res: Solid Earth.* 2017;122(11):8969–8989.
5. Ziegler MO, Heidbach O, Reinecker J, Przybycin AM, Scheck-Wenderoth M. A multi-stage 3-D stress field modelling approach exemplified in the Bavarian Molasse basin. *Solid Earth.* 2016;7(5):1365–1382.
6. Reiter K, Heidbach O. 3-D geomechanical–numerical model of the contemporary crustal stress state in the Alberta Basin (Canada). *Solid Earth.* 2014;5(2):1123–1149.
7. Fischer K, Henk A. A workflow for building and calibrating 3-D geomechanical models &ndash a case study for a gas reservoir in the north german basin. *Solid Earth.* 2013;4(2):347–355.
8. Guerra C, Fischer K, Henk A. Stress prediction using 1D and 3D geomechanical models of a tight gas reservoir—A case study from the lower Magdalena Valley Basin, Colombia. *Geomech Energy Environ.* 2019;19:100113.
9. Henk A. Perspectives of geomechanical reservoir models - why stress is important. *Oil Gas Eur Mag.* 2009;35:20–24.
10. Abbas A, Al-Asadi Y, Alsaba M, Flori R, Alhussainy S. Development of a geomechanical model for drilling deviated wells through the Zubair formation in southern Iraq. 2018.
11. Merey S. Geomechanical wellbore stability analysis for the wells drilled in the shallow sediments of the Mediterranean sea. *J Pet Sci Eng.* 2020;186:106714.
12. Dabab A, Abdulaziz A, manhalawi A, Abbas A, Alhussaini N. Managing wellbore instability through geomechanical modeling and wellbore stability analysis. 2020.
13. Dutta J, Sin A. Application of integrated reservoir geomechanics for well planning and drilling of nearly horizontal wells in a depleted reservoir of offshore Krishna-Godavari basin, India. 2015.
14. Rana R, Hansen K, Kandpal J, Kumar R, et al. Geomechanical models: Application to drilling in partially depleted fault blocks. 2016.
15. Smart K, Ofoegbu G, Morris A, McGinnis R, Ferrill D. Geomechanical modeling of hydraulic fracturing: Why mechanical stratigraphy, stress state, and pre-existing structure matter. *AAPG Bull.* 2014;98:2237–2261.
16. Kruszewski M, Hofmann H, Alvarez FG, Bianco C, et al. Integrated stress field estimation and implications for enhanced geothermal system development in Acozucol, Mexico. *Geothermics.* 2021;89:101931.
17. Moeck I, Kwiatek G, Zimmermann G. Slip tendency analysis, fault reactivation potential and induced seismicity in a deep geothermal reservoir. *J Struct Geol.* 2009;31(10):1174–1182.
18. Markou N, Papanastasiou P. Geomechanics in depleted faulted reservoirs. *Energies.* 2021;14(1).
19. Candela T, Osinga S, Ampuero J-P, Wassing B, et al. Depletion-induced seismicity at the Groningen gas field: Coulomb rate-and-state models including differential compaction effect. *J Geophys Res: Solid Earth.* 2019;124(7):7081–7104.
20. Fredrich J, Arguello J, Deitrick G, de Rouffignac E. Geomechanical modeling of reservoir compaction, surface subsidence, and casing damage at the belridge diatomite field. *SPE Reserv Eval Eng - SPE Res Eval Eng.* 2000;3.
21. Kidambi T, Hanegaonkar A, Dutt A, Kumar G. A fully coupled flow and geomechanics model for a tight gas reservoir: Implications for compaction, subsidence and faulting. *J Nat Gas Sci Eng.* 2017;38:257–271.
22. Dong K, Liu N, Chen Z, Huang R, Ding J, Niu G. Geomechanical analysis on casing deformation in Longmaxi shale formation. *J Pet Sci Eng.* 2019;177:724–733.
23. Van Wees J, Fokker P, Thienen-Visser K, Wassing B, et al. Geomechanical models for induced seismicity in the netherlands: Inferences from simplified analytical, finite element and rupture model approaches. *Neth J Geosci.* 2017;96:s183–s202.
24. COMSOL. *COMSOL Multiphysics Reference Manual.* Stockholm, Sweden: COMSOL AB; 2017.
25. Drozdowski G, Henscheid S, Hoth P, Juch D, et al. The pre-permian of NW-Germany - structure and coalification map. *Zeitschrift Der Deutschen Gesellschaft Für Geowissenschaften.* 2009;160:159–172.
26. Paas N. *Untersuchungen Zur Ermittlung Der Geochemischen Barriere Von Gesteinen Aus Dem Umfeld Untertägiger Versatzräume Im Steinkohlenbergbau Des Ruhrkarbons, Vol. 54.* DMT; 1997.
27. Hesemann J. *Die Ergebnisse Der Bohrung MÜNsterland, Vol. 1.* VS Verlag für Sozialwissenschaften; 1965.
28. DEKORP Research Group. Results of deep-seismic reflection investigations in the Rhenish massif. *Tectonophysics.* 1990;173(1):507–515. Seismic Probing of Continents and their Margins.
29. Wrede V. Thrusting in a folded regime: Fold accommodation faults in the Ruhr basin, Germany. *J Struct Geol.* 2005;27:789–803.
30. Brix M, Drozdowski G, Greiling R, Wolf R, Wrede V. The N variscan margin of the Ruhr coal district (western Germany): structural style of a buried thrust front? *Geologische Rundschau.* 1988;77(1):115–126.
31. Jansen F, von Kamp H, Kühn-Velten H, Kunz E, et al. Erläuterung zur Geologische Karte von Nordrhein-Westfalen 1:100000. In: *Blatt C 4710 Dortmund.* Krefeld, Germany: Geolog. Landesamt Nordrhein- Westfalen; 1986.
32. Drozdowski G, Grabert H, Hartkop-Fröder C, Jansen F, et al. Erläuterungen zur Geologischen Karte von Nordrhein-Westfalen 1:100 000. In: *Blatt C 4706 Düsseldorf-Essen.* Krefeld, Germany: Geolog. Landesamt Nordrhein-Westfalen; 2007.
33. Delvaux D, Moeys R, Stapel G, Petit C, et al. Paleostress reconstructions and geodynamics of the Baikal region, central Asia, part 2. Cenozoic rifting. *Tectonophysics.* 1997;282(1):1–38. Structural Controls on Sedimentary Basin Formation.
34. Balcewicz M, Ahrens B, Lippert K, Saenger EH. Characterization of discontinuities in potential reservoir rocks for geothermal applications in the Rhine-Ruhr metropolitan area (Germany). *Solid Earth.* 2021;12(1):35–58.
35. Gillhaus A, Götte T, Richter DK. Polyphase spät-diagenetische Dolomitbildung im mittel-bis oberdevonischen Massenkalk von Hagen-Hohenlimburg (Remscheid-Altener Sattel, Rheinisches Schiefergebirge). *Mitt Ges Geol Bergbaustud österr.* 2003;46:51–66.
36. Oncken O. Aspects of the reconstruction of the stress history of a fold and thrust belt (Rhenish Massif, Federal Republic of Germany). *Tectonophysics.* 1988;152(1):19–40.
37. Harnischmacher S. Quantification of mining subsidence in the Ruhr district (Germany). *Géomorphologie : Relief, Proc Environ.* 2010;16:261–274.
38. Brauner G. Spannungsuntersuchungen bei gebirgsschlaggefahr durch messung absoluter gebirgsspannungen. In: *Schlussbericht Zum Zuwendungsantrag.* RAG; 1976.
39. Müller W. Messung der absoluten Gebirgsspannung im Steinkohlebergbau. *Glückauf Forschungshefte.* 1989;50(2):105–112.
40. Müller W. The stress state in the Ruhr coalfield. Proc., 7th ISRM Congress; Aachen Germany: International Society for Rock Mechanics; 1991.
41. Stelling W, Rummel F. Messung von Primärspannungen durch Hydraulic Fracturing auf dem Bergwerk Haus Aden. *Mitteilung aus dem Markscheidewesen.* 1992;99(1):176–184.
42. Rummel F. Aufschluss und Stimulation kluftig / poroser Warmwasserspeicher zur Nutzung der Erdwärme an Standorten mit Nutzungspotential, Stimulation von Bohrungen in Kluft- wasserspeichern. In: *Abschlussbericht.* Bundesministerium fuer Wirtschaft und Technologie; 2003.
43. Rummel F, Weber U. Stress field in the coal mines of the ruhr coal district. In: *Géotechnique[001E01001].* Bochum 4630, Germany: U.S. symposium on rock mechanics. 34 (0 ; Madison, 1993-06-27), MeSy Geo-Messsysteme GmbH; 1993.
44. Rummel F, Weber U. *Compilation of Existing Hydrofrac In-situ Stress Data for the Ruhr Carboniferous.* Report (unpublished); Bochum: GEO-Mess-Systeme MESY GmbH; 1994.
45. Rudolph T, Melchers C, Minke A, Coldewey W. Gas seepages in Germany: Revisited subsurface permeabilities in the german mining district. *Aapg Bull - AAPG BULL.* 2010;94:847–867.
46. Reinecker J, Tingay M, Müller B, Plenkers K, Thielmann M. *Analyse der Bohrlochdaten von Nordrhein-Westfalen.* Report (unpublished); Krefeld, Germany: Landesamt Krefeld; 2008.
47. Heidbach O, Rajabi M, Cui X, Fuchs K, et al. The world stress map database release 2016: Crustal stress pattern across scales. *Tectonophysics.* 2018;744:484–498.
48. Baumann H. Regional stress field and Rifting in western Europe. In: ILLIES J, ed. *Mechanism of Graben Formation.* Elsevier; 1981:105–111. In: *Developments in Geotectonics;* vol. 17.
49. RUB. *RuhrNet - Seismic Network of the Ruhr-University Bochum.* Bochum, Germany: Ruhr University Bochum; 2007.
50. Bischoff M, Cete A, Fritschen R, Meier T. Coal mining induced seismicity in the Ruhr area, Germany. *Pure Appl Geophys.* 2010;167(1–2):63–75.
51. Hergert T, Heidbach O, Reiter K, Giger S, Marschall P. Stress field sensitivity analysis in a sedimentary sequence of the Alpine foreland, northern Switzerland. *Solid Earth.* 2015;6.
52. Simpson RW. Quantifying Anderson's fault types. *J Geophys Res: Solid Earth.* 1997;102(B8):17909–17919.
53. Jaeger J, Cook N, Zimmerman R. *Fundamental of rock mechanics.* 2007.
54. Morris A, Ferrill DA, Henderson D. Slip-tendency analysis and fault reactivation. *Geology.* 1996;24(3):275–278.
55. Ferrill D, Winterle J, Wittmeyer G, Sims D, Colton S, Armstrong A. Stressed rock strains groundwater at Yucca mountain, Nevada. In: *GSA Today, a Publication of the Geological Society of America, Vol. 2.* (5):1999:2–8.
56. Zoback MD. *Reservoir Geomechanics.* Cambridge University Press; 2007.
57. Reinewardt K-J, Rosensträter M, Enders G. Auffahrung der 7. Sohle des bergwerks prosper-haniel durch den krudenburg-sprung. *Glückauf.* 2009;145:38–46.

58. Thielemann T, Littke R. Examples of the methane exchange between litho- and atmosphere: the coal bearing Ruhr basin, Germany. In: Mastalerz M, Glikson M, Golding SD, eds. *Coalbed Methane: Scientific, Environmental and Economic Evaluation*. Dordrecht: Springer Netherlands; 1999:555–558.
59. Juch D, Roos W, Wolff M. Kohleninhaltefassung in den westdeutschen Steinkohlenlagerstätten. In: DROZDZEWSKI, G., JUCH, D., LOMMERZHEIM, AJ, ROOS, W.-F., WOLFF, M. & WREDE, V.: *Das Subvariscikum Nordwestdeutschlands*. 1994:189–307.
60. Juch D. Results of the resources assessment in the west German hard-coal deposits. In: *Proceedings of the XII. International Congress on the Carboniferous and Permian-Part, Vol. 2*. 1997:339–344.
61. MOVE. MOVE Suite; Version 2019.1.1. Edinburgh: Petroleum Experts Ltd.; 2019.
62. Drozdowski G. The Ruhr coal basin (Germany): structural evolution of an autochthonous foreland basin. *Int J Coal Geol*. 1993;23(1):231–250.
63. Gardner GHF, Gardner LW, Gregory AR. Formation velocity and density—the diagnostic basics for stratigraphic traps. *Geophysics*. 1974;39(6):770–780.
64. Jabs T. *Geomechanische Charakterisierung des flözführenden Oberkarbons unter zyklisch thermischer Belastung im gesättigten Zustand* (Ph.D. thesis). Ruhr University Bochum, Universitätsstraße 150, 44801 Bochum, DE; 2017.
65. Mullen M, Roundtree R, Turk G. A composite determination of mechanical rock properties for stimulation design (what to do when you don't have a sonic log). 2007.
66. International Geothermal Centre G. Well logging campaign 2016. 2016 Internal data (unpublished).
67. Marotta A, Bayer U, Thybo H, Scheck M. Origin of the regional stress in the north German basin: results from numerical modelling. *Tectonophysics*. 2002;360(1):245–264. Geophysical Investigations of the Trans-European Suture Zone II.
68. Zimmerman RW. *Compressibility of Sandstones*. Elsevier; 1991.
69. Wedewardt M. *Hydrochemie und Genese der Tiefenwässer im Ruhrrevier*. DMT-Berichte aus Forschung und Entwicklung; (39: 172 S). Germany: DMT; 1995.
70. Barton CA, Zoback MD, Moos D. Fluid flow along potentially active faults in crystalline rock. *Geology*. 1995;23(8):683–686.
71. Hickman S, Sibson R, Bruhn R. Introduction to special section: Mechanical involvement of fluids in faulting. *J Geophys Res*. 1995;1001:12831–12840.
72. Townend J, Zoback M. How faulting keeps the crust strong. *Geology*. 2000;28:399–402.
73. Davatzes NC, Eichhubl P, Aydin A. Structural evolution of fault zones in sandstone by multiple deformation mechanisms: Moab fault, southeast Utah. *GSA Bull*. 2005;117(1–2):135–148.
74. Davatzes NC, Aydin A. The formation of conjugate normal fault systems in folded sandstone by sequential jointing and shearing, waterpocket monocline, Utah. *J Geophys Res: Solid Earth*. 2003;108(B10).
75. Faulkner D, Jackson C, Lunn R, Schlische R, et al. A review of recent developments concerning the structure, mechanics and fluid flow properties of fault zones. *J Struct Geol*. 2010;32(11):1557–1575. Fault Zones.
76. Agosta F, Aydin A. Architecture and deformation mechanism of a basin-bounding normal fault in Mesozoic platform carbonates, central Italy. *J Struct Geol*. 2006;28(8):1445–1467.
77. Billi A, Salvini F, Storti F. The damage zone-fault core transition in carbonate rocks: implications for fault growth, structure and permeability. *J Struct Geol*. 2003;25(11):1779–1794.
78. Igbokwe OA, Mueller M, Bertotti G, Timothy JJ, Abah O, Immenhauser A. Morphology and topology of dolostone lithons in the regional carbonates fault zone, southern Spain. *J Struct Geol*. 2020;137:104073.
79. Homberg C, Hu J, Angelier J, Bergerat F, Lacombe O. Characterization of stress perturbations near major fault zones: insights from 2-D distinct-element numerical modelling and field studies (Jura mountains). *J Struct Geol*. 1997;19(5):703–718.
80. Meier T, Backers T, Dresen G, Gipper P. Stress, temperature, and pore pressure perturbations around a salt dome. 2015.
81. Lepillier B, Daniilidis A, Gholizadeh N, Bruna P-O, Kummerow J, Bruhn D. A fracture flow permeability and stress dependency simulation applied to multi-reservoirs, multi-production scenarios analysis. *Geotherm Energy*. 2019;7.
82. Gradmann S, Maystrenko Y, Keiding M, Olesen O. *3D Modelling of the In-Situ Stress Field in Nordland, Northern Norway*. Geological Survey of Norway, Trondheim, Norway; 2017.
83. Backers T, Meier T, Gipper P, Stephansson O. *Rock Mechanics – Confidence of SKB's models for predicting the occurrence of spalling*. Report number 2014:10; (ISSN: 2000-0456). Stockholm, Sweden: The Swedish Radiation Safety Authority; 2013.
84. Backers T, Meier T, Gipper P, Stephansson O. *Rock Mechanics – Assessing probability and extent of blind faults and fault-end growth around the KBS-3 repository at Forsmark*. Report number 2014:58; (ISSN: 2000-0456). Stockholm, Sweden: The Swedish Radiation Safety Authority; 2014.
85. Jeanne P, Guglielmi Y, Rutqvist J, Nussbaum C, Birkholzer J. Field characterization of elastic properties across a fault zone reactivated by fluid injection. *J Geophys Res: Solid Earth*. 2017;122(8):6583–6598.
86. Duda M, Ahrens B, Kroll K, Gilbert J. Thermomechanical effects of seasonal thermal energy storage in former subsurface mining structures. In: *EGU General Assembly Conference Abstracts*. 2019:13108. In: EGU General Assembly Conference Abstracts.
87. Ahrens B, Gilbert J, Kroll K, Duda M. Thermomechanical characterization of subsurface seasonal thermal energy storage in the Ruhr metropolitan area. In: *Der Geothermiekongress DGK*. 2018. In: Der Geothermiekongress DGK.
88. Duda M, Renner J. The weakening effect of water on the brittle failure strength of sandstone. *Geophys J Int*. 2012;192(3):1091–1108.
89. Stöckhert F, Solibida C, Alber M. Hydraulic fractures in discontinuous, anisotropic and heterogeneous rock - a lab study. In: *ISRM EUROCK*. 2020.
90. Verberne B, He C, Spiers C. Frictional properties of sedimentary rocks and natural fault gouge from the Longmen Shan fault zone, Sichuan, China. *Bull Seismol Soc Am*. 2010;100.
91. Zoback MD, Kohli AH. *Unconventional Reservoir Geomechanics: Shale Gas, Tight Oil, and Induced Seismicity*. Cambridge University Press; 2019.
92. Cao L, Yao Y, Cui C, Sun Q. Characteristics of in-situ stress and its controls on coalbed methane development in the southeastern Qinshui Basin, north China. *Energy Geosci*. 2020;1(1):69–80.
93. Konon A, Wyglądała M, Haluch A, Rybak-Ostrowska B, Cyz M, Malinowski M. Using seismic and well data to determine processes of folding in the pomeranian segment of the Caledonian foredeep basin, Poland. *Mar Pet Geol*. 2021;124:104804.
94. Bruno MS, Winterstein DF. Some influences of stratigraphy and structure on reservoir stress orientation. *Geophysics*. 1994;59(6):954–962.
95. Heidbach O, Reinecker J, Tingay M, Müller B, et al. Plate boundary forces are not enough: Second- and third-order stress patterns highlighted in the world stress map database. *Tectonics*. 2007;26(6).
96. Drozdowski G. Die Wurzel der Osning-Überschiebung und der Mechanismus herzynischer Inversionsstörungen in Mitteleuropa. *Geologische Rundschau (1910. Print)*. 1988.
97. Brücker C, Preuß A. The future of underground spatial planning and the resulting potential risks from the point of view of mining subsidence engineering. *Int J Mining Sci Technol*. 2020;30(1):93–98. Special issue on ground control in mining in 2019.
98. Gombert P, Sracek O, Koukouzas N, Gzyl G, et al. An overview of priority pollutants in selected coal mine discharges in Europe. *Mine Water Environ*. 2018;38.
99. Hahne C, Schmidt R. *Die Geologie Des Niederrheinisch-Westfälischen Steinkohlengebietes*. Verlag Glückauf GmbH; 1982.
100. Heidbach O, Ziegler M, Morawietz S. Geomechanical assessment of potential for induced seismicity. In: *EGU General Assembly Conference Abstracts*. 2020:10514. In: EGU General Assembly Conference Abstracts.
101. Ziegler M, Heidbach O. Quantification and reduction of uncertainties in 3D stress models. In: *EGU General Assembly Conference Abstracts*. 2020:2821. In: EGU General Assembly Conference Abstracts.
102. Gibowicz JS, Kijko A. *An Introduction to Mining Seismology*. 1994.
103. Alber M, Fritschen R. Rock mechanical analysis of a M1=4.0 seismic event induced by mining in the Saar district, Germany. *Geophys J Int*. 2011;186:359–372.
104. Peña-Castro AF, Kemna KB, Harrington RM, Roth MP, Liu Y. Source mechanism of seismicity generated by one of the last active coal mines in Germany before its closure. In: *AGU Fall Meeting Abstracts, Vol. 2018*. 2018:S21A-08.
105. Kruszewski M. Modelled three-dimensional in situ stress state and fault reactivation risk in the Ruhr region. *Fordatis*. 2022. URL <http://dx.doi.org/10.24406/fordatis/205>.